

Recent changes in tropospheric water vapor over the Arctic as assessed from radiosondes and atmospheric reanalyses

Mark C. Serreze,¹ Andrew P. Barrett,¹ and Julienne Stroeve¹

Received 29 December 2011; revised 10 April 2012; accepted 11 April 2012; published 16 May 2012.

[1] Changes in tropospheric water vapor over the Arctic are examined for the period 1979 to 2010 using humidity and temperature data from nine high latitude radiosonde stations north of 70°N with nearly complete records, and from six atmospheric reanalyses, emphasizing the three most modern efforts, MERRA, CFSR and ERA-Interim. Based on comparisons with the radiosonde profiles, the reanalyses as a group have positive cold-season humidity and temperature biases below the 850 hPa level and consequently do not capture observed low-level humidity and temperature inversions. MERRA has the smallest biases. Trends in column-integrated (surface to 500 hPa) water vapor (precipitable water) computed using data from the radiosondes and from the three modern reanalyses at the radiosonde locations are mostly positive, but magnitudes and statistical significance vary widely between sites and seasons. Positive trends in precipitable water from MERRA, CFSR and ERA-Interim, largest in summer and early autumn, dominate the northern North Atlantic, including the Greenland, Norwegian and Barents seas, the Canadian Arctic Archipelago and (on the Pacific side) the Beaufort and Chukchi seas. This pattern is linked to positive anomalies in air and sea surface temperature and negative anomalies in end-of-summer sea ice extent. Trends from ERA-Interim are weaker than those from either MERRA or CFSR. As assessed for polar cap averages (the region north of 70°N), MERRA, CFSR and ERA-Interim all show increasing surface-500 hPa precipitable over the analysis period encompassing most months, consistent with increases in 850 hPa air temperature and 850 hPa specific humidity. Data from all of the reanalyses point to strong interannual and decadal variability. The MERRA record in particular shows evidence of artifacts likely introduced by changes in assimilation data streams. A focus on the most recent decade (2001–2010) reveals large differences between the three reanalyses in the vertical structure of specific humidity and temperature anomalies.

Citation: Serreze, M. C., A. P. Barrett, and J. Stroeve (2012), Recent changes in tropospheric water vapor over the Arctic as assessed from radiosondes and atmospheric reanalyses, *J. Geophys. Res.*, 117, D10104, doi:10.1029/2011JD017421.

1. Introduction

[2] Water vapor strongly influences atmospheric dynamics and the hydrologic cycle through latent heat transport and diabatic heating. Water vapor is also the most abundant greenhouse gas. As the equilibrium vapor pressure of water vapor increases rapidly with temperature, warming (or cooling) induced by a climate forcing will be amplified through water vapor feedback [e.g., Soden *et al.*, 2002]. The strength of this feedback is a key determinant of the planet's

equilibrium climate sensitivity. Assessing and understanding variability and change in atmospheric water vapor is hence an important element of climate change research.

[3] Ross and Elliott [2001] used radiosonde data from land stations to examine Northern Hemisphere trends for two periods, 1958–1995 and 1973–1995. At most stations, the surface to 500 hPa column-integrated water vapor (precipitable water), specific humidity and dewpoint at 850 hPa show positive trends, allied with increases in air temperature. Europe is an exception, where temperature increased over the analyzed period but humidity decreased slightly. Increases in water vapor were found to be stronger and more uniform over North America than over Eurasia. For the subset of stations with longer records from 1958 to 1995, trends are small, indicating that most of the increase in water vapor occurred since 1973.

[4] Over the oceans after 1987, satellite-based estimates of precipitable water are available from algorithms applied to data from the Special Sensor Microwave/Imager [Wentz,

¹National Snow and Ice Data Center, Cooperative Institute for Research in Environmental Sciences, University of Colorado Boulder, Boulder, Colorado, USA.

Corresponding author: M. C. Serreze, National Snow and Ice Data Center, Cooperative Institute for Research in Environmental Sciences, University of Colorado Boulder, Campus Box 449, Boulder, CO 80309-0449, USA. (serreze@kryos.colorado.edu)

1997]. Using these data, *Trenberth et al.* [2005] report an increase of $1.3\% \pm 0.3\%$ (0.40 ± 0.09 mm) per decade in precipitable water for the global ocean as a whole over the period 1988–2003, with both the spatial structure and temporal variability of trends closely related to rising sea surface temperature. Similar to findings by *Ross and Elliott* [2001], the main area where positive trends are absent is over Europe. *Dai* [2006] used observations of surface air temperature, dewpoint temperature and air pressure from land stations and ships to examine trends in surface specific and relative humidity over the period 1975–2005. Statistically significant upwards trends were found in the annual global mean (60°S – 75°N) and Northern Hemisphere specific humidity (0.06 and 0.08 g kg^{-1} per decade), with accompanying upward trends in surface air temperature. The specific humidity trend in the Southern Hemisphere was found to be positive but statistically insignificant. However, in contrast to findings by *Ross and Elliott* [2001], and pointing toward strong impacts of decadal variability, the largest positive trends in surface specific humidity were found to occur over Eurasia, in association with strong warming. As argued by *Philipona et al.* [2005] on the basis of high correlations between increasing cloud-free downward longwave radiation at the surface and changes in absolute humidity, this warming over Europe can be largely explained by water vapor feedback. Using the radiosonde network, *McCarthy et al.* [2009] report moistening across the extratropical Northern Hemisphere lower and middle troposphere on the order of 1 to 5% per decade, with little or no change in relative humidity over the same period. *Dai et al.* [2011], using a homogenized radiosonde data record for the period 1973–2008, confirm an increase in tropospheric water vapor globally, with middle to lower tropospheric relative humidity remaining relatively stable.

[5] The conclusion that can be drawn from these and other studies is a general increase in tropospheric water vapor over recent decades, but with considerable spatial and temporal variability. Upper-tropospheric water vapor is expected to be an especially important feedback mechanism, and satellite data show a distinct radiative signature of increased humidity in this part of the atmosphere [*Soden et al.*, 2005]. *Solomon et al.* [2010], by contrast, find that satellite-derived global averaged stratospheric water vapor concentrations declined by about 10% over the 2000–2009 decade, acting to slow the rate of increase in global average surface temperature over that period by about 25% compared to the warming that would have occurred due only to carbon dioxide and other greenhouse gases. They also provide evidence that stratospheric water vapor increased over the period 1980–2000, enhancing surface warming over that period.

[6] The present paper focuses on changes in tropospheric water vapor over the Arctic, a region in the midst of rapid environmental change. The past two decades have seen pronounced rises in surface and lower-tropospheric air temperature over the Arctic, larger than for the Northern Hemisphere as a whole, strongly expressed over the Arctic Ocean during the cold season [*Serreze et al.*, 2009; *Screen and Simmonds*, 2010a, 2010b; *Overland and Wang*, 2010]. Assessment of the satellite data record (1979–present) reveals downward linear trends in Arctic sea ice extent for all

months, largest at the end of the melt season in September (12% per decade through 2011) [*Stroeve et al.*, 2008] (<http://nsidc.com/arcticseaicenews/>). The ice cover is also thinning [*Maslanik et al.*, 2007; *Nghiem et al.*, 2006]. While part of the observed Arctic autumn and winter warming is related to variability in atmospheric circulation and other factors, reduced sea ice extent has played a role by allowing for strong energy transfers from the ocean to the atmosphere [*Serreze et al.*, 2009; *Screen and Simmonds*, 2010b]. The seasonality and vertical structure of recent warming over the Arctic Ocean are broadly consistent with projections of Arctic amplification of air temperature changes in climate model simulations [e.g., *Manabe and Stouffer*, 1980; *Holland and Bitz*, 2003; *Serreze et al.*, 2009]. A recent synthesis of the observational record for the pan-Arctic terrestrial drainage points to intensification of the hydrologic cycle, with increases in annual precipitation, evapotranspiration, and river discharge to the Arctic Ocean [*Rawlins et al.*, 2010].

[7] Given a warmer atmosphere with more open ocean water, one expects corresponding increases in tropospheric water vapor storage in the Arctic troposphere, acting as a feedback to further the warming. *Rinke et al.* [2009] examined changes in Arctic water vapor for the period 1958–2001 based on data from the European Centre for Medium-Range Weather Forecasts (ECMWF) ERA-40 reanalysis [*Uppala et al.*, 2005], and simulations from a regional model. While finding a predominance of positive trends in all seasons, the pattern is heterogeneous, with significant positive trends over the western Arctic in summer and a small negative trend over the East Siberian Sea in winter. *Francis and Hunter* [2007] report on positive springtime trends (over the period 1979–2005) in downward longwave radiation over the Arctic Ocean surface based on satellite retrievals from the Television Infrared Observation Satellite (TIROS) Operational Vertical Sounder (TOVS), which they link to both changing cloud conditions and increased atmospheric water vapor. Analysis of data from the ECMWF ERA-Interim reanalysis [*Dee et al.*, 2011] for 1989–2009 by *Screen and Simmonds* [2010b] suggests that the pronounced cold season temperature rises over the Arctic Ocean have been attended by an increase in the latent heat flux from the ocean to the atmosphere.

[8] While these studies offer evidence for increasing tropospheric water vapor in the Arctic, there is a clear need for a more comprehensive evaluation. We examine Arctic changes for the period 1979–2010, using humidity and temperature data from nine high-latitude radiosonde sites north of 70°N with nearly complete records and from a suite of atmospheric reanalyses. Our focus is primarily on the monthly as opposed to seasonal time scale. As will become evident as results are presented, there can be important differences in Arctic climate conditions from month to month that would be masked by the use of seasonal means. While we examine linear trends in humidity, we also use Hovmoller diagrams and cross sections to address decadal variability.

[9] The radiosonde data represent both raw profiles from the Integrated Global Radiosonde Archive (IGRA) [*Durre et al.*, 2006] (<http://www.ncdc.noaa.gov/oa/climate/igra/>) and profiles that have been subjected to a series of adjustments in an effort to improve homogenization

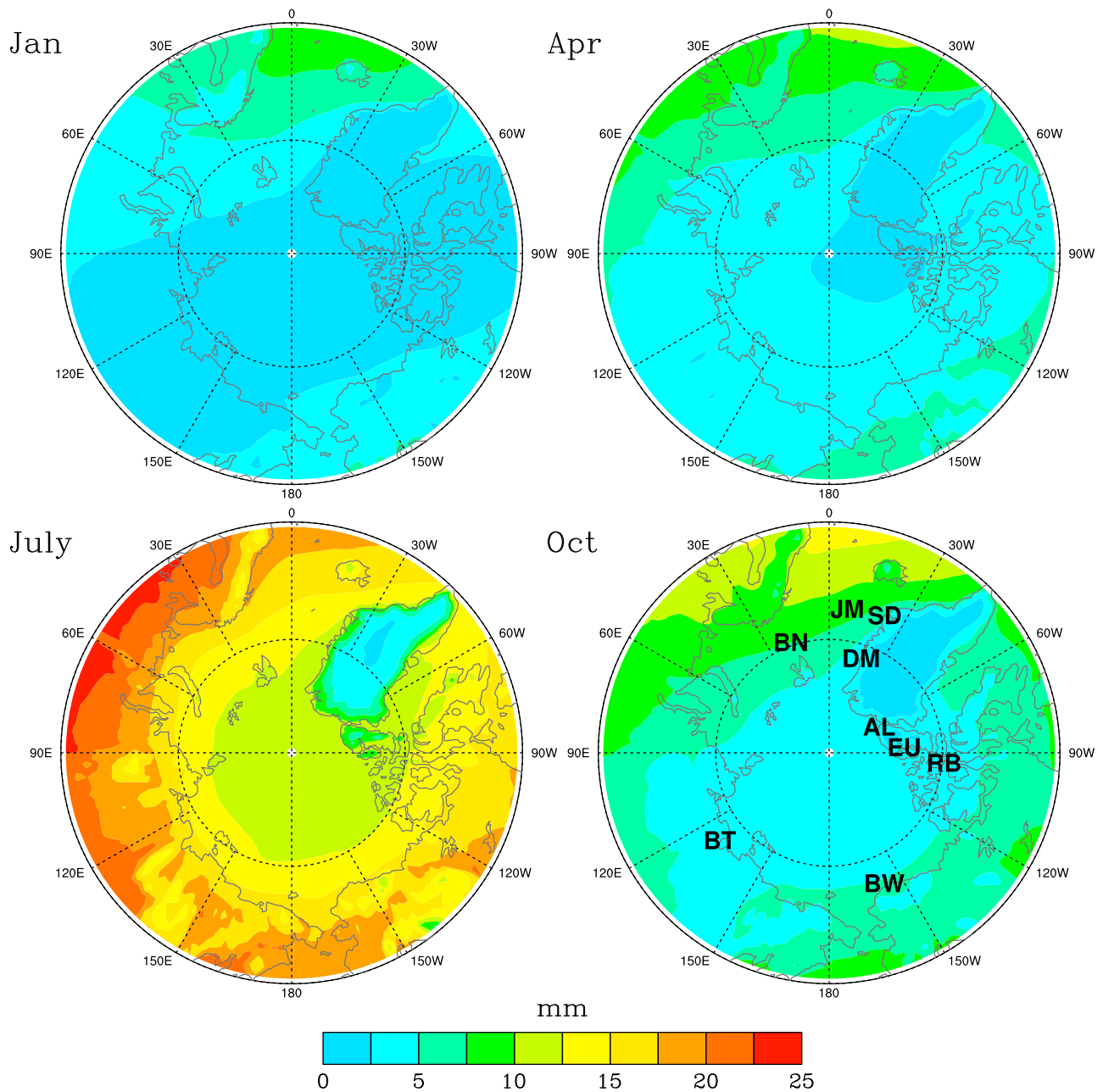


Figure 1. Annual mean surface to 500 hPa precipitable water for the region north of 60°N from the MERRA reanalysis for the four mid-season months, based on data from 1979 to 2010. Also plotted on the map for October is the location of the nine radiosonde sites. The letter codes are: JM –Jan Mayen; BN – Bjornoya; SD – Scoresbysunde; DM – Danmarkshavn; BT – Bukhta Tiski; BW – Barrow, AL – Alert; EU – Eureka; RB – Resolute Bay.

[Dai *et al.*, 2011]. Of the six reanalyses used, emphasis is placed on the three newest efforts, the National Aeronautics and Space Administration Modern Era Retrospective-Analysis for Research and Applications (MERRA) [Rienecker *et al.*, 2011]) (<http://gmao.gsfc.nasa.gov/merra/>; see also M. Bosilovich, 2008, NASA’s Modern Era Retrospective-analysis for Research and Applications: Integrating Earth observations, 2008, <http://www.earthzine.org/2008/09/26/nasas-modern-era-retrospective-analysis>, the National Oceanic and Atmospheric Administration CFSR (Climate Forecast System Reanalysis) [Saha *et al.*, 2010] ([\[noaa.gov/cfsr/\]\(http://noaa.gov/cfsr/\)\) and ERA-Interim, hereon referred to as ERA-I \[Dee *et al.*, 2011\] \(<http://www.ecmwf.int/research/era/do/get/era-interim>\)\). The remaining three used for comparison are ERA-40 \(ERA-I is an effort to prepare for ECMWF’s next generation reanalysis that will replace ERA-40\), the Japanese 25-year reanalysis JRA-25 \[Onogi *et al.*, 2007\] and the original NCEP/NCAR \(National Centers for Environmental Prediction/National Center for Atmospheric Research\) effort \[Kalnay *et al.*, 1996\], hereafter termed NCEP-1. The year 1979 corresponds to the advent of modern satellite](http://cfs.ncep.</p>
</div>
<div data-bbox=)

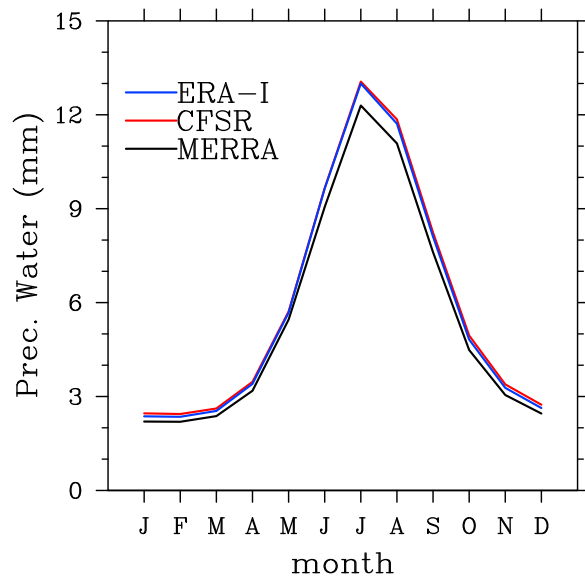


Figure 2. Mean annual cycle of precipitable water (surface to 500 hPa) for the polar cap (the region north of 70°N) based on MERRA, CFSR and ERA-I data for the period 1979–2010.

data streams for ingest into the reanalysis systems. The ERA-40 record terminates in 2002.

[10] To familiarize the reader with the basic seasonal and spatial patterns of water vapor in the Arctic, Figure 1 shows mean fields of precipitable water (surface to 500 hPa) for the four mid-season months from MERRA for the region north of 60°N. For January, values are highest (up to 10 mm, note that $\text{mm} = \text{kg m}^{-2}$) over the North Atlantic and extending eastward, corresponding to relatively high tropospheric temperatures and open ocean waters. By comparison, January values over the central Arctic Ocean, Canadian Arctic Archipelago, Greenland and Siberia are 2.5 mm or less, reflecting the combination of low air temperatures and (for Greenland) the high elevation of the ice sheet surface (locally > 3000 m). Precipitable water peaks in July at about 25 mm near the edge of the mapped domain over northern Eurasia, with values over the central Arctic Ocean of 10–12.5 mm. These values compare to a global annual average (integrated to the top of the atmosphere) of around 25 mm. Also shown in Figure 1 is the location of the nine radiosonde stations, which sample from both the drier and moister parts of the Arctic. These sites were chosen as the daily records have fewer than 10% missing cases for the period 1979–2010.

[11] Mean seasonal cycles of surface to 500 hPa precipitable water from MERRA, CFSR and ERA-I, averaged for the polar cap domain, taken as the region north of 70°N, follow in Figure 2. Consistent with earlier studies of Arctic water vapor based on radiosonde data [e.g., Serreze *et al.*, 1995; Walsh *et al.*, 1995], the reanalyses depict about a factor of five range in precipitable water between the winter minimum and the July maximum. MERRA is somewhat dry compared to either ERA-I or CFSR, most pronounced in summer. Serreze *et al.* [1995] find that depending on the month, the column from the surface to 500 hPa accounts for 89–96% of Arctic water vapor. For January, about 70% of

precipitable water is found below the 700 hPa level, dropping to about 50% in July.

2. Data

2.1. Radiosonde Profiles

[12] An ongoing challenge in water vapor analyses is obtaining accurate and consistent data. This is particularly true for the polar regions. While radiosonde profiles are often viewed as a gold standard, these data are subject to error from a number of sources, including inaccurate humidity measurements at low temperatures and humidity, changes through time in the reporting of humidity at low humidity and temperatures, and that different countries have used different instrument types which have in turn changed through time [e.g., Elliott and Gaffen, 1991; Garand *et al.*, 1992; McCarthy *et al.*, 2009]. In 2003 globally there were 14 different radiosonde types in use [Wang *et al.*, 2003].

[13] The IGRA, assembled by the National Climatic Data Center, contains soundings from 11 different sources, subjected to comprehensive quality control to address format problems, eliminate duplicate levels within soundings, physically implausible values, temporal and vertical inconsistencies in temperature and other problems. Durre *et al.* [2006] provide a comprehensive overview. We make use of both the original IGRA records for the nine sites and homogenized records assembled from the IGRA by A. Dai and colleagues [Dai *et al.*, 2011]. Briefly, they used two statistical tests to detect change points in dewpoint depression (DPD) that are most apparent in histograms and occurrence frequencies in daily DPD frequency. These comprise a variant of the Kolmogorov-Smirnov (K-S) test for changes in the distributions and a penalized maximal F test for mean shifts in the occurrence frequency for different bins of DPD. Before applying these tests, the data were adjusted to address a number of known problems in radiosonde archives; this includes estimating missing DPD records for cold ($T < -30^\circ\text{C}$) and dry (DPD artificially set to 30°C) conditions using empirical relationships at each station between anomalies of temperatures and vapor pressure derived from recent observations when DPD reports are available under these conditions. The data were then detrended and adjusted using a quantile matching algorithm so that the earlier segments of the records have histograms comparable to the latest record segment.

[14] To examine vertical profiles, we use the 1–2 times daily homogenized records at each station at mandatory reporting levels up to 300 hPa (1000, 850, 700, 500, 400 and 300 hPa) compiled into monthly means, first converting DPD values in each sounding into specific humidity. Precipitable water (surface to 500 hPa) is calculated from the raw IGRA records using both the significant and mandatory level DPD data; precipitable water based on mandatory and significant levels is already calculated as part of the Dai *et al.* homogenized data set. The Dai *et al.* data set extends through 2008.

2.2. Atmospheric Reanalyses

[15] Atmospheric reanalyses are retrospective forms of numerical weather prediction using a fixed model and data assimilation system. Analyzed fields (analyses) such as pressure heights, winds, temperature and specific humidity

Table 1. Characteristics of the Six Atmospheric Reanalyses Used in the Present Study

Model	MERRA	CFSR	NCEP-I	ERA-40	ERA-I	JRA-25
Resolution ^a	1/2 lat. × 2/3 lon. (~55 km)	T382 (~38 km)	T62 (~210 km)	T159 (~125 km)	T255 (~79 km)	T106 (~125 km)
Levels	72	64	28	60	60	40
Time Span	1979–2011	1979–present	1948–present	1958–2002	1979–present	1979–present
Assimilation Scheme	3D-Var/IAU	3D-Var	3D-Var	3D-Var	4D-Var	3D-Var
Bias Correction	VarBC	VarBC	Static	Static	VarBC	VarBC
Humidity Assimilated	Yes	Yes	No	Yes	In troposphere but not in Stratosphere	Yes
Sea Ice Concentration threshold	Prescribed 50%	Assimilated 15%	Prescribed 55%	Prescribed 20%	Prescribed 20%	Prescribed 55%
Albedo Reference	Fixed <i>Rienecker et al.</i> [2011]	Varies with surface <i>Saha et al.</i> [2010]	Fixed <i>Kalnay et al.</i> [1996]	Seasonal prescribed <i>Uppala et al.</i> [2005]	Seasonal prescribed <i>Dee et al.</i> [2011]	Fixed <i>Onogi et al.</i> [2007]

^aResolution refers to spectral resolutions (numbers preceded by T) for all models except MERRA. Resolutions in brackets refer to grid spacing.

at standard atmospheric levels represent the blending of a short-term atmospheric forecast with observations from radiosondes, satellites, aircraft reports and other sources. The blending of forecasts and observations is performed during analysis cycles. Each analysis cycle consists of collecting, selecting, and quality control of observations available within the analysis window, typically 6h; blending observations with a first guess of the state of the atmosphere (the short-term forecast) using a statistical interpolation scheme; balancing the analysis to control fast moving gravity waves that may dominate the forecast; and integrating the forecast model forward in time to the beginning of the next analysis cycle using the new analysis as initial conditions for the forecast step. The new forecast is used as the first guess for the next analysis cycle.

[16] Up to this time, global reanalyses have almost exclusively used a variational analysis approach as their statistical interpolation scheme. In variational analysis, a cost function – the distance between a first guess field and observations – is minimized to obtain the best blending of observations and the first guess field. While the above discussion provides a general framework, different reanalysis projects have tackled some or all of the steps in the analysis cycles in different ways. The devil is often in the details. Advances in computing power, changes in observational networks and advances in the science of data assimilation have all led to improvements in reanalysis.

[17] Table 1 summarizes features of the six global atmospheric reanalyses used in our study. NCEP-1, the oldest listed system, has the lowest horizontal resolution, sharply contrasting with the much higher resolution of MERRA, CFSR and ERA-I. All of the reanalyses employ a 3D-Var (three dimensional variational analysis) assimilation system except ERA-I, which employs 4D-Var with a 12h analysis cycle. In 3D-Var, the analysis is obtained by minimizing the distance between the first guess and observations within an analysis window, i.e., the aim is to get the best estimate of atmospheric conditions for a single analysis time. In 3D-Var, observations within the analysis window but further away in time from the time of the first guess might be discarded. 4D-Var extends the 3D-Var approach to include the time dimension; the aim is to find initial conditions (the analysis) such that the evolution of the forecast best matches observations through time in the analysis window. This approach

allows more observations to be used than in 3D-Var [*Dee et al.*, 2011]. Unique to MERRA is the Incremental Analysis Update (IAU) procedure. In most variational analysis approaches, analysis increments – the difference between the analysis and first guess – are added to the first guess states before the next forecast is made. This rapid adjustment in model states can result in unstable behavior in the model; in particular the “spindown” of precipitation in the tropics [*Andersson et al.*, 2005]. The IAU in MERRA adds analysis increments gradually to the forecast using tendencies. This approach has reduced the spindown problem with precipitation and has improved the stratospheric circulation [*Rienecker et al.*, 2011].

[18] The older NCEP-1 system assimilates derived profiles from satellite data as opposed radiances in the more modern systems. Retrievals estimate vertical temperature and humidity profiles from satellite data through a series of empirical and statistical relationships. Raw radiances by contrast are direct satellite measurements of radiation; while the use of radiances is more computationally expensive it eliminates errors associated with the retrieval process [*Bromwich et al.*, 2007]. NCEP-1 assimilates satellite retrievals of temperature but not humidity according to *Rinke et al.* [2009]. An important step in using satellite radiance observations in data assimilation is bias correction. Biases depend on atmospheric conditions at the time of observations, radiative transfer schemes, and the instrument and channel used, among other factors [*Dee et al.*, 2011]. In ERA-40 and JRA-25, parameters of biases correction procedures are estimated offline [*Rienecker et al.*, 2011]. In MERRA, CFSR and ERA-I, these parameters are estimated using a Variational Bias Correction (VarBC) procedure that is part of the analysis cycle. This can be thought of as an inter-calibration of satellite radiance observations using all other observations in the analysis cycle and the model first guess where observations are sparse [*Dee et al.*, 2011].

[19] In most of the reanalyses listed in Table 1, sea surface temperatures and sea ice are prescribed boundary conditions. In CFSR sea ice extent and thickness are prognostic variables, with extent updated by assigning open water to grid points for which the observed sea ice concentration is less than 15%. The sea surface temperature and sea ice data sets used in all reanalyses are either the same or derived from the same satellite data sources using

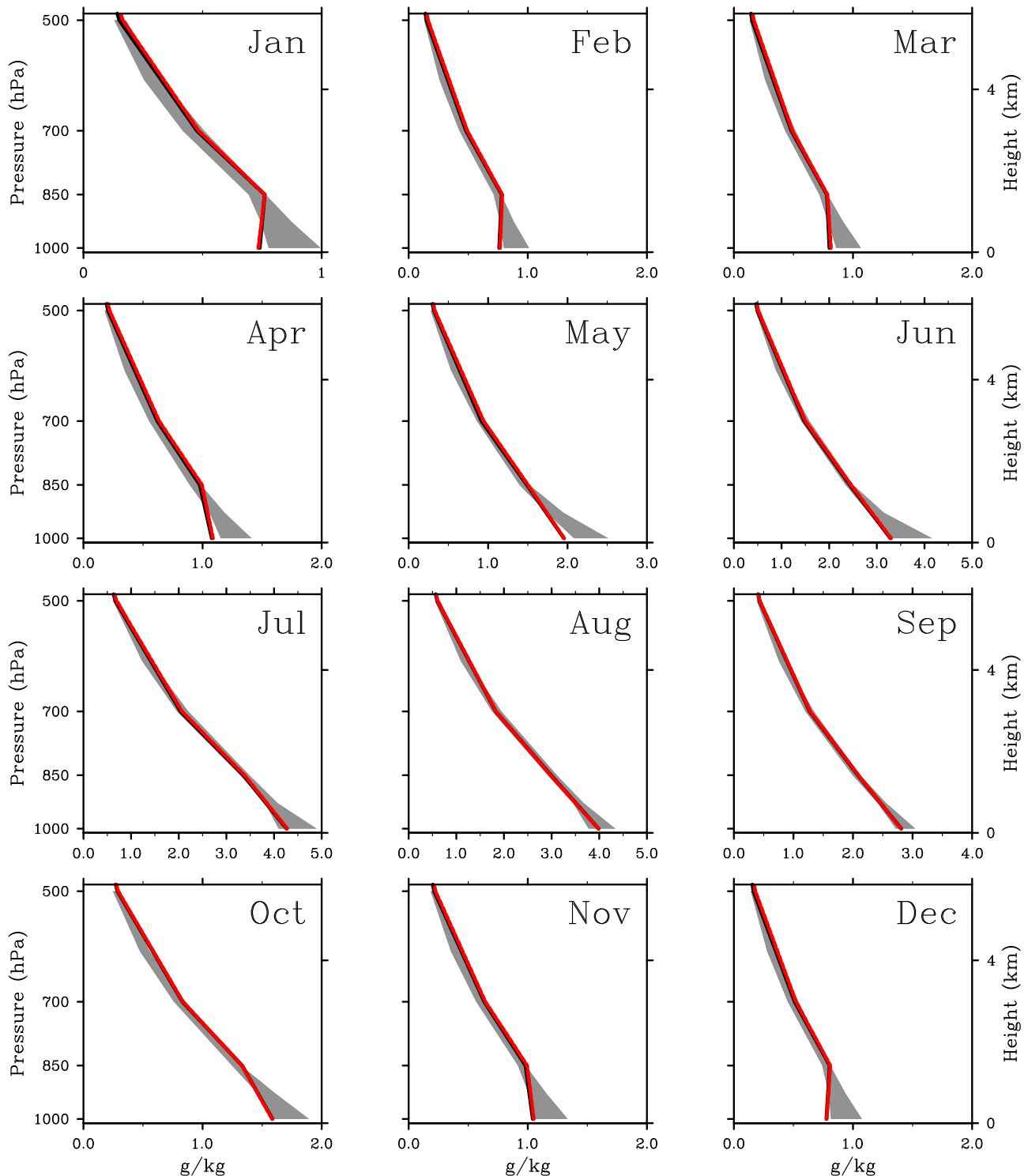


Figure 3. Comparison of monthly mean profiles of specific humidity from the radiosonde stations and reanalyses. Means are for the period 1979–2001 common to all reanalyses. The mean profiles based on the nine radiosonde sites are shown by the red line (raw IGRA records) and black line (homogenized IGRA records). The gray shading shows the range in specific humidity between the six reanalyses based on data at the grid point closest to the radiosonde sites.

similar algorithms. However, there are differences in how these data sets are used. ERA-40 and ERA-I classify ocean grid cells with sea ice concentrations less than 20% as open water. CFSR uses a 15% ice concentration

threshold. The other reanalyses use a 50% or 55% ice concentration threshold. Ice surface albedo values and whether or not a fixed or seasonally varying value is used depends on the reanalysis. Choice of the albedo scheme

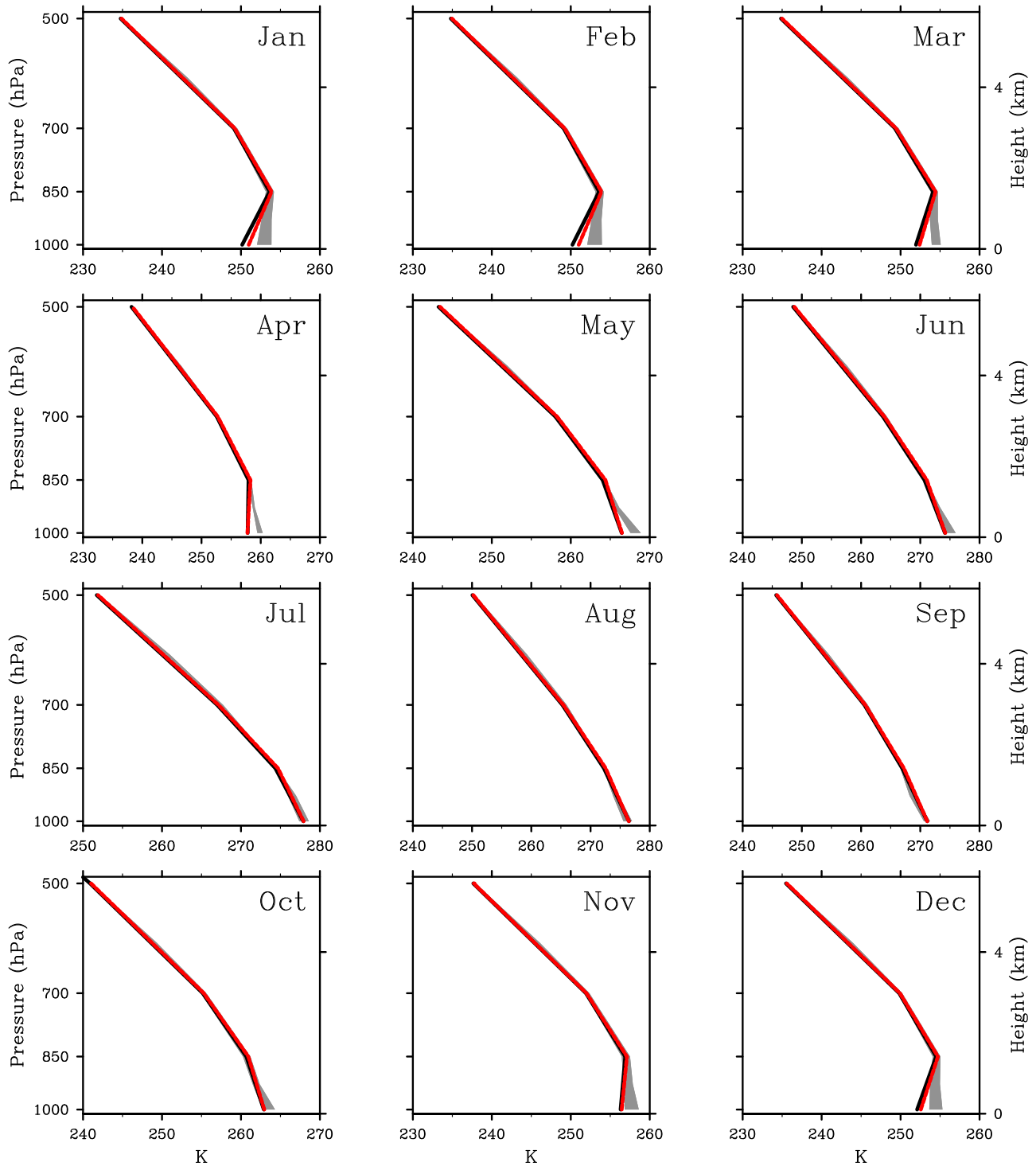


Figure 4. Comparison of monthly mean profiles of air temperature from the radiosonde stations and reanalyses. Means are for the period 1979–2001 common to all reanalyses. The mean profiles based on the nine radiosonde sites are shown by the red line (raw IGRA records) and black line (homogenized IGRA records). The gray shaded shading shows the range in air temperature between the six reanalyses based on data at the grid point closest to the radiosonde sites.

can strongly influence the surface heat budget [Cullather and Bosilovich, 2011]. Further details on individual reanalyses can be found in the references included in Table 1 and references therein.

2.3. Reanalysis Bias Assessments

[20] In any climate study using reanalysis data, one must be aware of biases with respect to observations and non-climatic features in time series related to changes in

Table 2. Biases in 1000 hPa Specific Humidity (%) With Respect to Radiosonde Data

	Jan	Feb	Mar	Apr	May	Jun	Jul	Aug	Sep	Oct	Nov	Dec	MAB ^a
CFSR	31.3	28.9	28.4	23.4	16.4	9.0	1.8	2.3	6.2	17.6	22.4	33.9	18.5
ERA-40	16.0	12.6	14.0	15.2	13.4	10.8	5.8	3.5	1.8	7.4	8.2	19.2	10.6
ERA-I	14.4	11.7	11.0	7.9	7.5	10.5	7.4	4.4	2.3	6.1	7.6	17.6	9.0
JRA25	11.7	9.8	11.3	17.1	17.7	8.9	1.5	-0.7	-1.2	2.7	5.1	14.8	8.5
NCEP-1	39.6	38.0	39.2	32.2	29.1	26.5	15.6	9.3	9.3	21.4	30.2	45.2	28.0
MERRA	7.1	7.5	8.6	11.8	8.2	0.7	-2.6	-4.9	-1.6	1.6	2.4	8.6	5.5

^aMean absolute bias.

assimilated data streams. While as evident from Figure 2 and further developed in this paper there are differences in the depiction of climate variables from different reanalyses, there are some biases in specific humidity and air temperature qualitatively common to all of the reanalyses.

[21] To assess these biases, for each month, data from the radiosonde stations were aggregated together at each mandatory level (1000, 850, 700 and 500 hPa) to get group mean profiles, one set using the homogenized records and another using the raw IGRA records. Mean profiles were then compiled for each reanalysis individually, using data for the grid point closest to the radiosonde sites. For each month we then plotted the average radiosonde-based profiles of specific humidity along with the range in mean specific humidity at each level between the six reanalyses. All averages are for the period 1979–2001 common to all of the reanalyses.

[22] With respect to both specific humidity (Figure 3) and temperature (Figure 4), mean profiles from the raw and homogenized IGRA records are nearly indistinguishable from each other. Winter months are characterized by low-level temperature and humidity inversions [Devasthale *et al.*, 2011]. Compared to the IGRA profiles, the reanalyses are characterized by a general pattern of overly high specific humidity and temperature extending from the surface to the 850 hPa level, most pronounced during the cold season; none of the reanalyses reproduce the observed wintertime humidity and temperature inversions. Agreement with the radiosonde data is by contrast quite good at higher levels. This suggests that the reanalyses are either not assimilating the radiosonde data at low levels or are giving these data a low weight. Only for August does the spread in the reanalysis humidity estimates below the 850 hPa level clearly straddle the IGRA values. Agreement with the IGRA profiles is much better during the summer months.

[23] Tables 2 and 3 summarize monthly biases in specific humidity and temperature for the six reanalyses with respect to the homogenized IGRA data at the 1000 hPa level (where the biases are largest). Biases in specific humidity are expressed as a percentage of the mean specific humidity from the radiosondes. Also given is the annual mean %

absolute bias. MERRA has the smallest humidity biases overall, while NCEP and CFSR have the largest, which as expected from Figure 3 are most prominent in the Arctic cold season. Differences between MERRA, CFSR and ERA-I in the magnitude, sign and seasonality of low-level humidity biases are reflected in the seasonal cycles of precipitable water for the polar cap shown in Figure 2. MERRA and JRA-25 have small negative biases (too dry compared to the radiosondes) for summer months and September, most notable for MERRA in August. Temperature biases have a seasonal structure similar to the humidity biases, being generally smallest in summer and largest in the cold season. CFSR and ERA-I show the largest positive cold-season temperature biases. MERRA, NCEP-1 and JRA-25 are in turn too cool in summer and early autumn. Overall, as is evident in the annual root mean square error (RMSE), MERRA has the smallest temperature biases. These results must be viewed with the caveat that they are based on a small number of radiosonde observations that have their own errors.

[24] Bromwich *et al.* [2007] examined impacts of changing data streams in a tropospheric assessment of the performance of NCEP-1, ERA-40, and JRA-25 for both the Arctic and Antarctic. Notably, they identify a middle troposphere cold bias in ERA-40 over the central Arctic Ocean related to assimilation of HIRS data (High Resolution Infrared Radiation Sounder aboard NOAA satellites). In 1997, in an effort to reduce precipitation biases in ERA-40 in the tropics, changes were made to the thinning, selection and quality control of the HIRS data, and the Arctic cold bias disappeared. Cullather and Bosilovich [2011] find that the MERRA moisture budget components are sensitive to introduction of data from the Advanced Microwave Sounding Unit (AMSU) introduced in November 1998. Another significant change was introduction of the AIRS (Advanced Infrared Sounder) instrument in 2002. The AIRS instrument flies on the NASA Aqua satellite along with the AMSU-A, CERES and AMSR-E instruments.

[25] Our use of a suite of reanalyses along with radiosonde data provides us with a spread of estimates of changes in Arctic water vapor. We are aware of other data sets. After

Table 3. Biases in 1000 hPa Temperature (K) With Respect to Radiosonde Data

	Jan	Feb	Mar	Apr	May	Jun	Jul	Aug	Sep	Oct	Nov	Dec	RMS
CFSR	2.92	3.02	2.60	1.90	1.01	0.28	-0.07	0.12	0.34	1.34	1.98	2.62	1.87
ERA-40	1.90	1.94	1.86	2.33	2.29	1.70	0.64	0.56	0.35	0.80	1.06	1.75	1.58
ERA-I	2.72	2.66	2.11	1.46	0.80	0.80	0.22	0.31	0.44	1.18	1.81	2.64	1.69
JRA25	1.75	1.77	1.78	2.36	2.19	1.07	0.05	-0.17	-0.48	-0.09	0.52	1.38	1.39
NCEP-1	1.66	1.80	1.85	1.78	1.71	1.11	-0.04	-0.18	-0.57	-0.09	0.62	1.43	1.28
MERRA	1.04	1.33	1.38	1.52	1.06	0.07	-0.50	-1.18	-0.55	-0.16	0.33	0.95	0.97

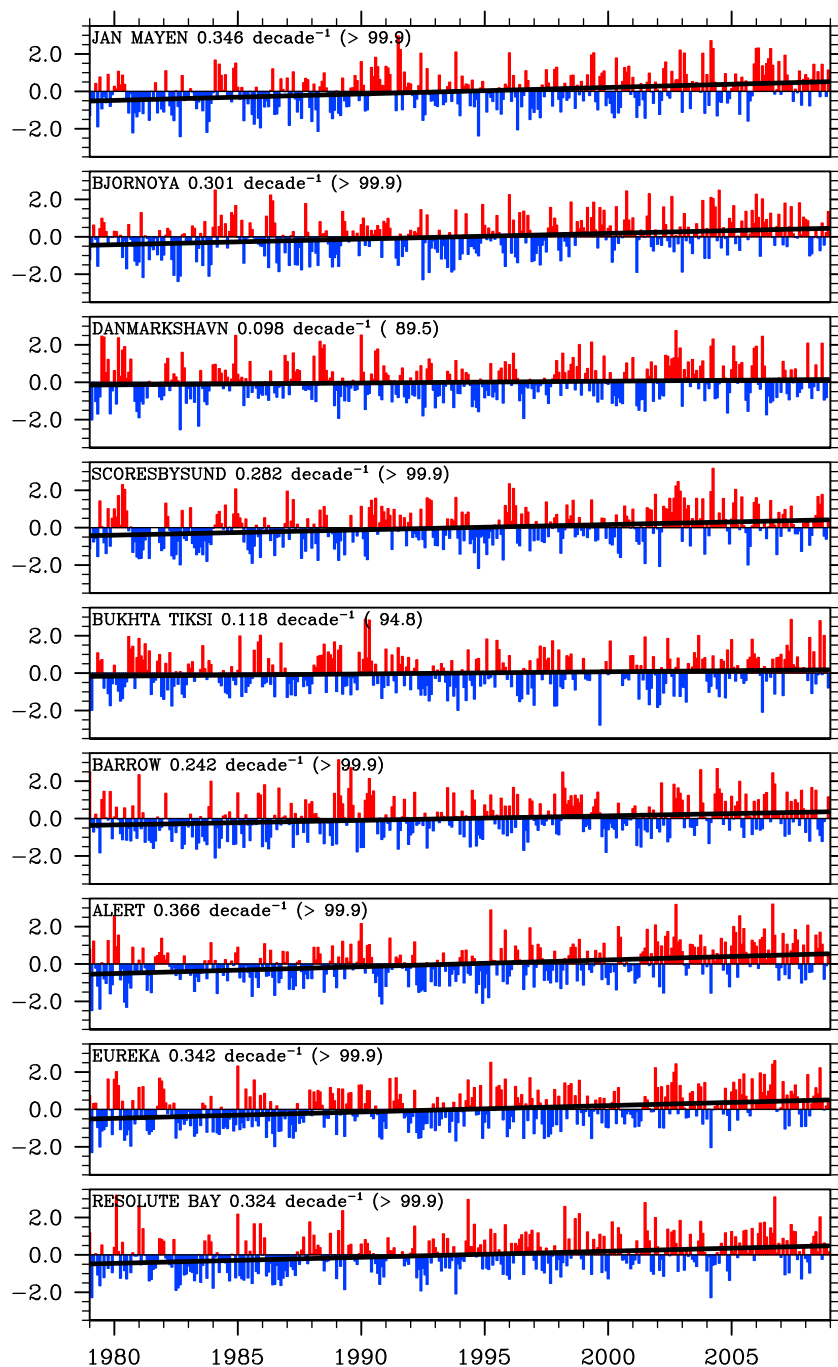


Figure 5. Time series (1979–2010) of monthly standardized anomalies (z-scores) in surface to 500 hPa precipitable water at the nine radiosonde sites, along with the linear trend line (shown in black), slope (z score per decade) and (in parentheses) the statistical significance.

1987, satellite-based estimates of precipitable water are available based on algorithms applied to data from the Special Sensor Microwave/Imager, but only for the open ocean [Wentz, 1997] and are of limited value on the Arctic. As discussed, Francis and Hunter [2007, and references therein] have made use of an Arctic data set based in TOVS data. The NASA NVAP (NASA Water Vapor Project) data set combines satellite retrievals from TOVS, SSM/I and radiosonde data [Randel et al., 1996; Simpson et al., 2001], but concerns have been raised

regarding how records from instruments on various satellites have been merged [Trenberth et al., 2005].

3. Trends at the Radiosonde Sites

[26] The homogenized records from the radiosonde stations are summarized in Figure 5 as monthly standardized anomaly time series (z-scores) of surface-500 hPa precipitable water. The z-scores are based on the means and standard deviations for each month for the period 1979–2008.

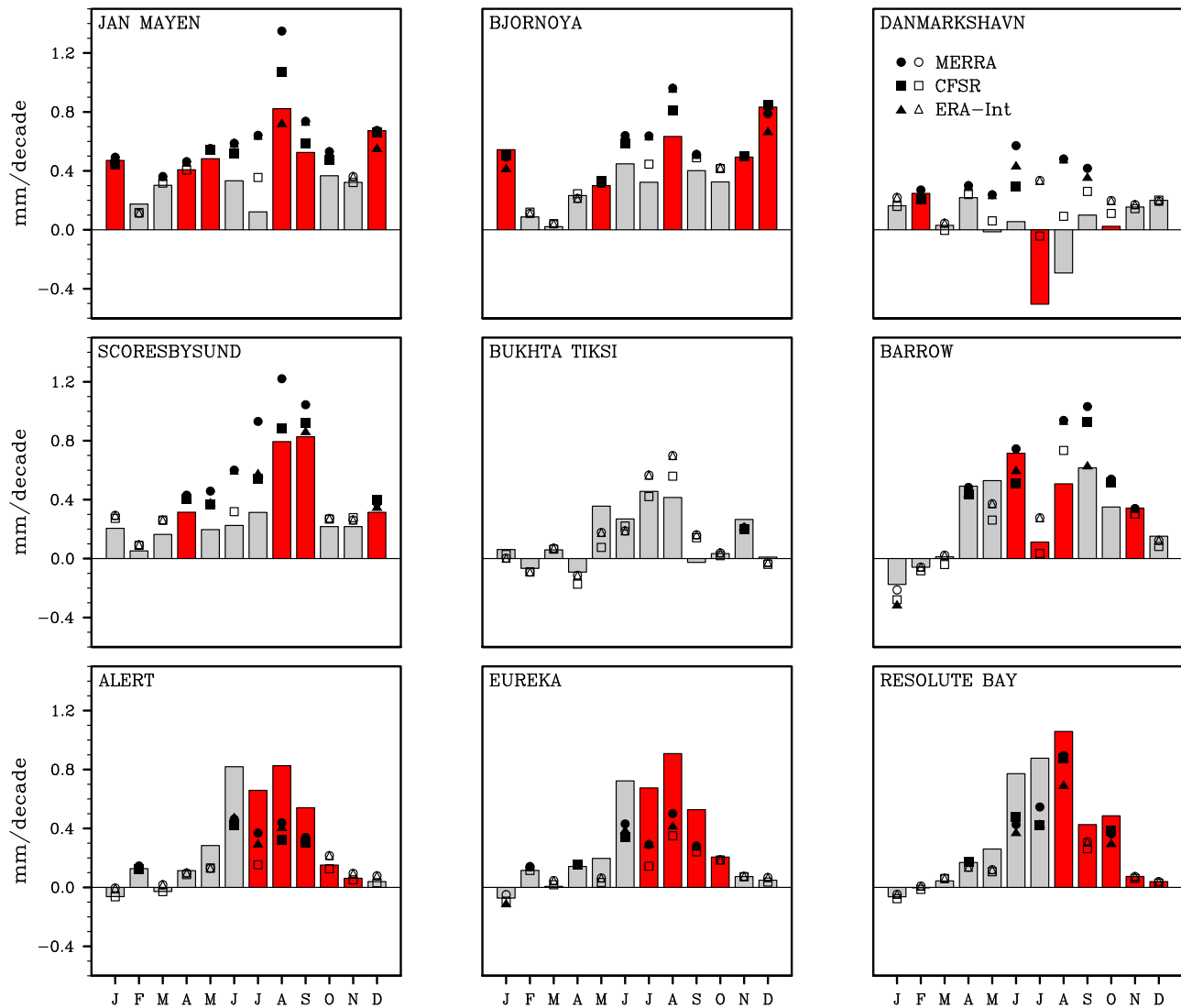


Figure 6. Comparison of monthly trends in surface to 500 hPa precipitable water based on data from radiosonde stations (bars) and from the MERRA, CFSR and ERA-I reanalyses at the grid points closest to the radiosonde sites (symbols). Red bars (radiosonde data) and closed symbols (reanalysis data) depict statistically significant trends at the 90% level or greater.

While there is obviously strong variability from month to month, there are small upward trends in the z-scores time series at all sites, all of which are statistically significant at the 95% confidence level except for Danmarkshavn (89.5%) and Bukhta (94.8%). The same analysis performed in the raw IGRA data yields essentially the same results.

[27] Linear trends (mm per decade) over the 1979–2008 period in surface to 500 hPa precipitable water at each site from the homogenized IGRA records are broken down by month in Figure 6 along with trends from the MERRA, CFSR and ERA-Interim reanalyses based on data from the grid points closest to the sites. With few exceptions, the radiosonde-based trends are positive, but magnitudes and statistical significance vary widely depending on the month and station. The three sites representing the northern Canadian Arctic Archipelago (Alert, Eureka, Resolute Bay; see Figure 1) show the strongest trends in summer through earlier autumn (the largest is about 1.06 mm per decade for

Resolute Bay in August), with very small and insignificant trends in the winter months. The other sites show little seasonality in trends; interestingly, Danmarkshavn shows a statistically significant negative trend in July of -0.50 mm per decade. There are no significant radiosonde-based trends at the Bukhta Tiski site located along the Siberian Arctic coast (Figure 1). Trends from the three reanalyses are also mostly positive, but are variously larger or smaller than the radiosonde-based estimates. We see no evidence of trends from any one of the reanalyses being systematically stronger or weaker compared to the others.

[28] As discussed earlier, all of the reanalyses have a moist bias at and near the surface (where most of the water vapor resides), suggesting that reanalyses are either not assimilating the radiosonde data at low levels or are giving these data a low weight. Given that radiosondes represent a key data stream, it is natural to question how much credence one should place on the reanalysis-based trends. That trends

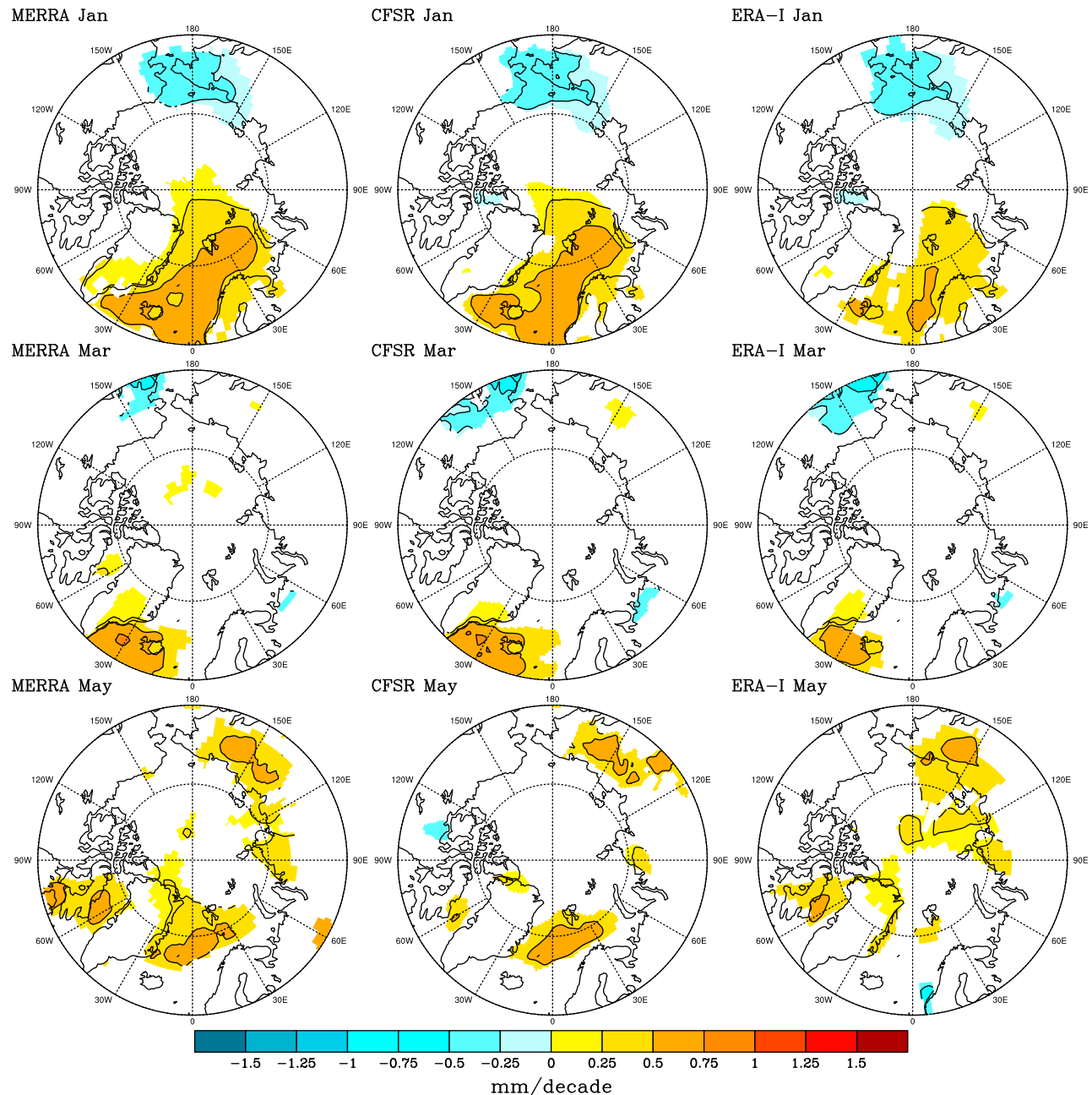


Figure 7. Spatial pattern of linear trends in surface to 500 hPa precipitable water for the period 1979–2010 for alternate months (January, March, May, July, September, and November) from MERRA, CFSR and ERA-I. Trends for all colored areas are statistically significant at the 90% level or greater.

based on radiosonde data and reanalyses, in most cases, agree in sign but not necessarily in magnitude, suggests that increasing water vapor in the Arctic is a robust result but that there is uncertainty in the rate of this increase.

4. Spatiotemporal Patterns of Reanalysis Trends

4.1. Map Patterns

[29] Figure 7 shows spatial patterns of linear trends (1979–2010) in surface to 500 hPa precipitable water for

alternate months (January, March, May, July and September, November) based on data from MERRA, CFSR and ERA-I. Trends in all colored areas are statistically significant at the 90% level or greater. Trends in white areas are not significant. The maps cover the region 60°N to the pole. While the trend patterns from the three reanalyses are overall similar, trends in ERA-I are generally of smaller magnitude.

[30] For January, the three reanalyses show significant positive trends over the Atlantic sector of the Arctic.

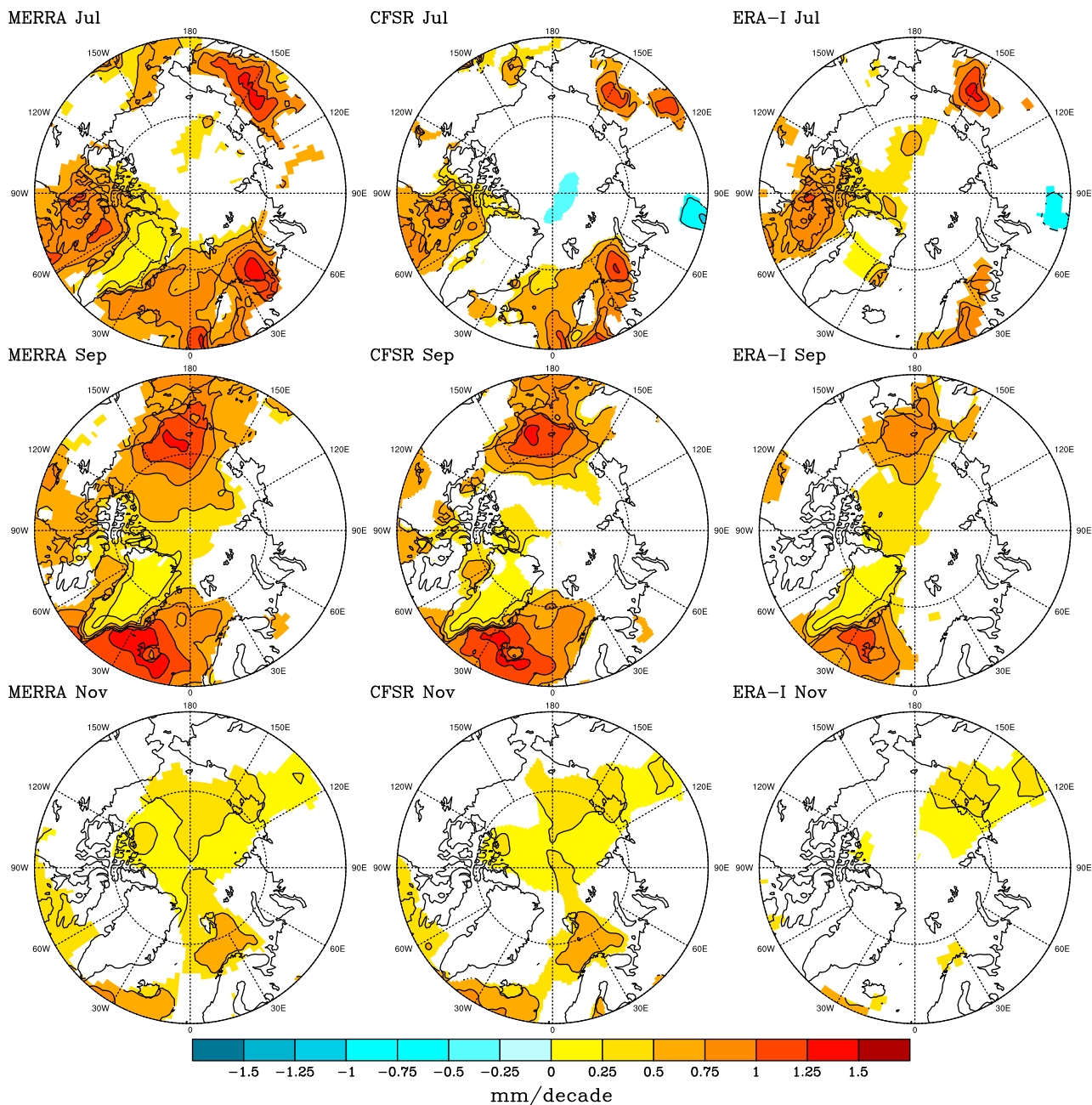


Figure 7. (continued)

Climatologically, this is the warmest part of the Arctic. As shown in a recent analysis of 925 hPa temperatures based on NCEP-1 data [Serreze *et al.*, 2011], these relatively high tropospheric temperatures are in large part maintained

by diabatic heating by the warm open ocean, which counters predominant cold advection associated with the passage of weather systems along the North Atlantic cyclone track. Serreze *et al.* [2011] find that positive

Figure 8. Cross sections based on MERRA data by height (vertical axis, up to 300 hPa) and latitude (horizontal axis) of (left column) anomalies in specific humidity for the decade 2001–2010 relative to 1979–2010 means (middle column), anomalies in specific humidity for 2001–2010 expressed as a percent change relative to 1979–2010 means, and (right column) anomalies in air temperature. The cross sections are for a transect extending from 60°N along the date line northward to 90°N and then along the prime meridian southward to 60°N. Anomalies in specific humidity exceeding 0.1 g kg⁻¹ (absolute values) are shown in color, as are anomalies larger than $\pm 5\%$. For temperature, anomalies that exceed 0.5°C in absolute magnitude are shown in color. The cross sections are provided for alternate months (January, March, May, July, September, and November).

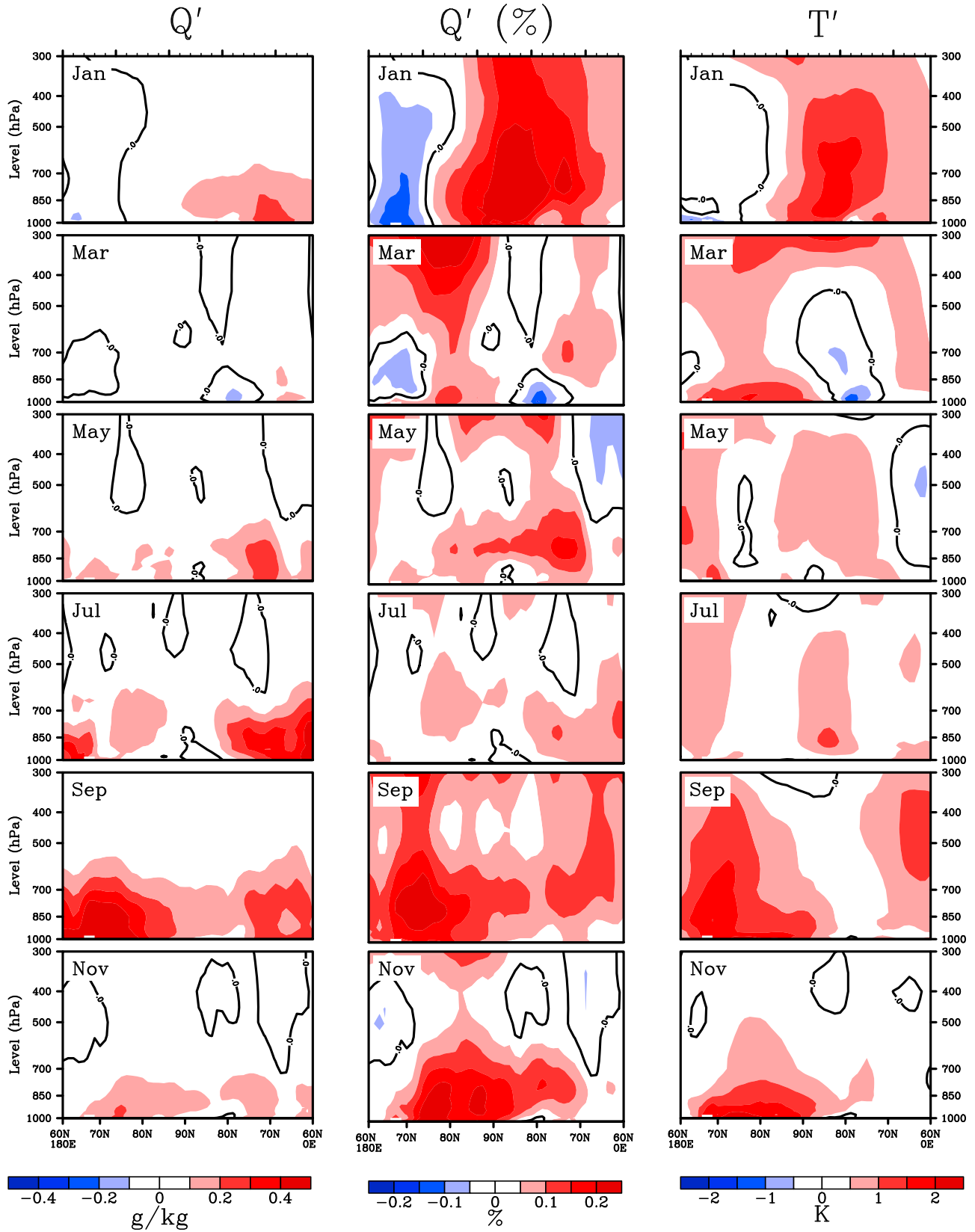


Figure 8

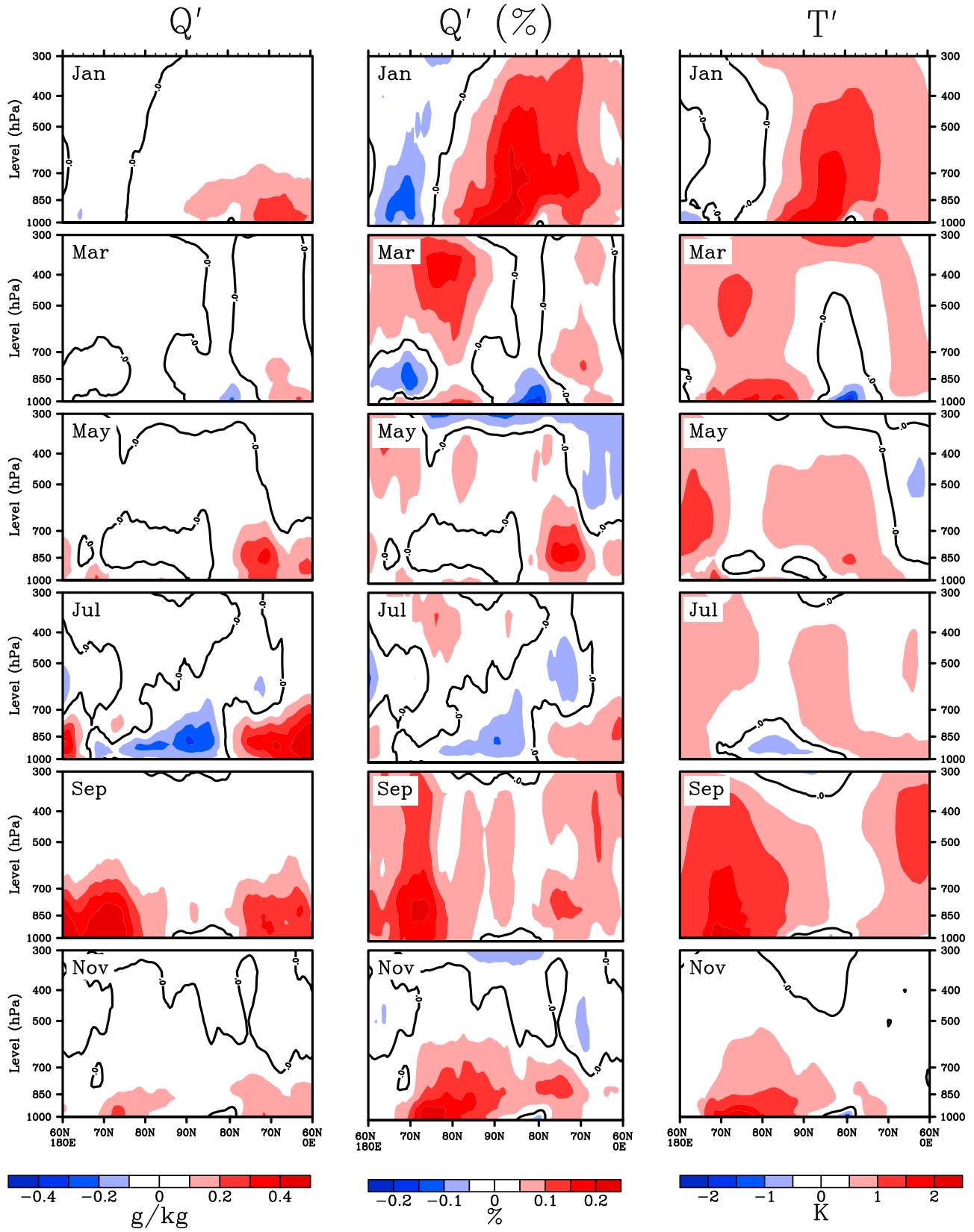


Figure 9

winter temperature anomalies in the Atlantic sector for the decade 2000–2009 compared to 1979–2009 means (also seen in MERRA, CFSR and ERA-I data), consistent with trends in precipitable water shown in Figure 7, can be linked to a combination of anomalous positive temperature advection tied to an anomalous southerly wind component, reduced sea ice extent, and positive sea surface temperature anomalies. The negative trends in January precipitable water centered over eastern Eurasia are consistent with a circulation shift in atmospheric circulation featuring an increased frequency of winds with a northerly component.

[31] Few significant trends are depicted for March; all three reanalyses show that these are limited to parts of the northern North Atlantic (positive) and Alaska (negative). The lack of widespread trends in this month is consistent with the radiosonde analysis (Figure 6). While the three reanalyses agree that nearly all significant trends in May trends are positive, the region of positive trends over the northern North Atlantic in MERRA and CFSR is not depicted in ERA-I.

[32] Turning to July, MERRA shows positive trends over the Atlantic side of the Arctic, the Canadian Arctic Archipelago, as well as eastern Siberia. Locally, trends exceed 1.5 mm per decade. The absence of trends over the central Arctic Ocean is consistent with the effects of a melting ice surface, which limits change in the surface saturation vapor pressure. CFSR shows the same basic spatial pattern as MERRA, but with generally smaller trends. ERA-I again departs from the other two reanalysis in the lack of substantial trends over the Atlantic side of the Arctic Ocean. In all three reanalysis, significant trends are most widespread and strongest in August (not shown), and are especially pronounced in each product over the Canadian Arctic Archipelago. This agrees with the radiosonde analysis, which shows strong positive August trends for Eureka, Alert and Resolute Bay.

[33] While all of the reanalyses show positive North Atlantic trends in September, the most interesting feature of this month, consistent across the products, is a region of positive trends centered over the Beaufort and Chukchi seas. In MERRA and CSFR these locally exceed 1.5 mm per decade. This feature corresponds with where negative trends in end-of-summer summer sea ice extent have been most pronounced. By September, the solar radiation flux to the surface is small, and there are strong transfers of heat from the anomalous open water to the atmosphere, manifested as strong positive anomalies in lower tropospheric air temperatures and hence a larger vapor carrying capacity of the air [Serreze *et al.*, 2009; Screen and Simmonds, 2010a, 2010b]. This region of strong positive trends is also present in the three reanalyses in August.

The feature is not present in November, by which time the area is largely covered by new ice, limiting ocean-atmosphere energy exchanges. MERRA and CFSR depict significant positive trends over the northern North Atlantic and Central Arctic in this month. ERA-I by contrast shows few trends. Stroeve *et al.* [2011], in a study using JRA-25 reanalysis, also noted increased cyclone associated precipitation and precipitable water in the northern North Atlantic in autumn in recent decades.

[34] It is instructive to examine Figures 8, 9, and 10, which depict the vertical structure of recent anomalies in specific humidity and temperature for each reanalysis. Vertical cross sections were compiled for alternative months along a transect extending from 60°N along the date line northward to 90°N and then along the prime meridian southward to 60°N. Along the date line, this transect cuts across the longitude corresponding to some of the largest negative anomalies in September sea ice extent in the Chukchi Sea. Along the prime meridian the transect extends into the open waters of the northern North Atlantic. For the 2001–2010 decade, data from the MERRA reanalysis (Figure 8) depict positive anomalies in specific humidity exceeding 0.1 g kg⁻¹ that extend above the 700 hPa level in summer and early autumn. The largest anomalies are not necessarily at the surface. The predominance of positive anomalies in specific humidity is linked to positive anomalies in air temperature. When humidity anomalies are examined in terms of percent change, a different picture emerges. Some of the largest positive percent changes are depicted in the middle and upper troposphere. For January, the MERRA data point to drying on the Pacific side of the Arctic, reflecting the recent atmospheric circulation anomalies centered over eastern Eurasia noted earlier with respect to Figure 7.

[35] The vertical structures of recent anomalies in specific humidity from the CFSR (Figure 9) are generally quite similar to those in MERRA, one notable exception being July, when CFSR depicts a region of negative anomalies, largest (about -2 g kg⁻¹) near the pole at about the 850 hPa level. As with MERRA, some of the largest percent changes in specific humidity for the 2001–2010 decade are located in the middle and upper troposphere. The vertical structure of temperature anomalies depicted in these two reanalyses is similar.

[36] A somewhat different pattern emerges for ERA-I (Figure 10). Note the especially pronounced difference between CFSR and ERA-I for July; the region of negative anomalies in CFSR centered near the pole is entirely absent in ERA-I, which instead depicts positive anomalies peaking at about the 850 hPa level.

[37] To provide a different perspective, the Hovmoller plots comprising Figure 11 summarize MERRA anomalies

Figure 9. Cross sections based on CFSR data by height (vertical axis, up to 300 hPa) and latitude (horizontal axis) of (left column) anomalies in specific humidity for the decade 2001–2010 relative to 1979–2010 means (middle column), anomalies in specific humidity for 2001–2010 expressed as a percent change relative to 1979–2010 means, and (right column) anomalies in air temperature. The cross sections are for a transect extending from 60°N along the date line northward to 90°N and then along the prime meridian southward to 60°N. Anomalies in specific humidity exceeding 0.1 g kg⁻¹ (absolute values) are shown in color, as are anomalies larger than +/-5%. For temperature, anomalies that exceed 0.5°C in absolute magnitude are shown in color. The cross sections are provided for alternate months (January, March, May, July, September, and November).

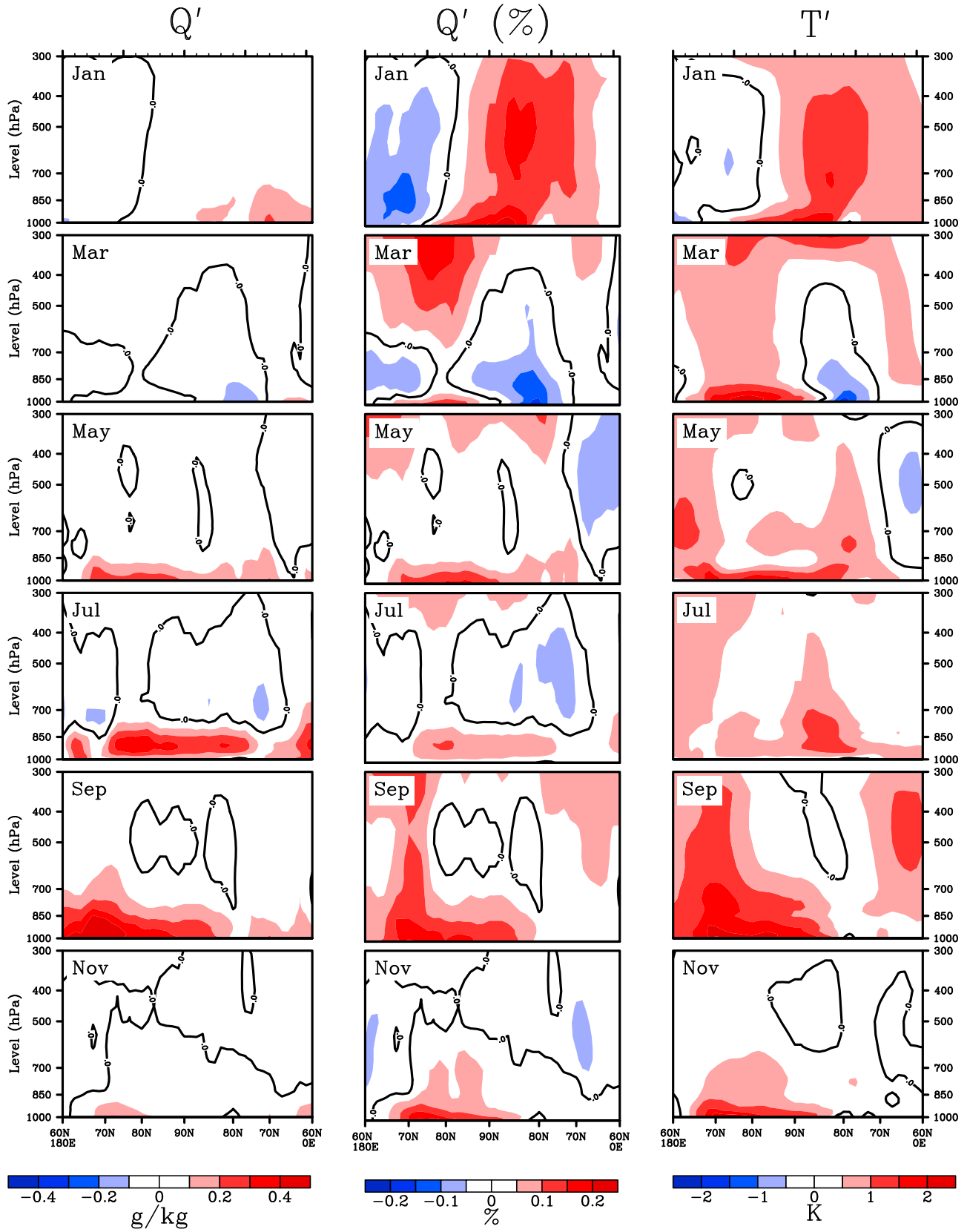


Figure 10

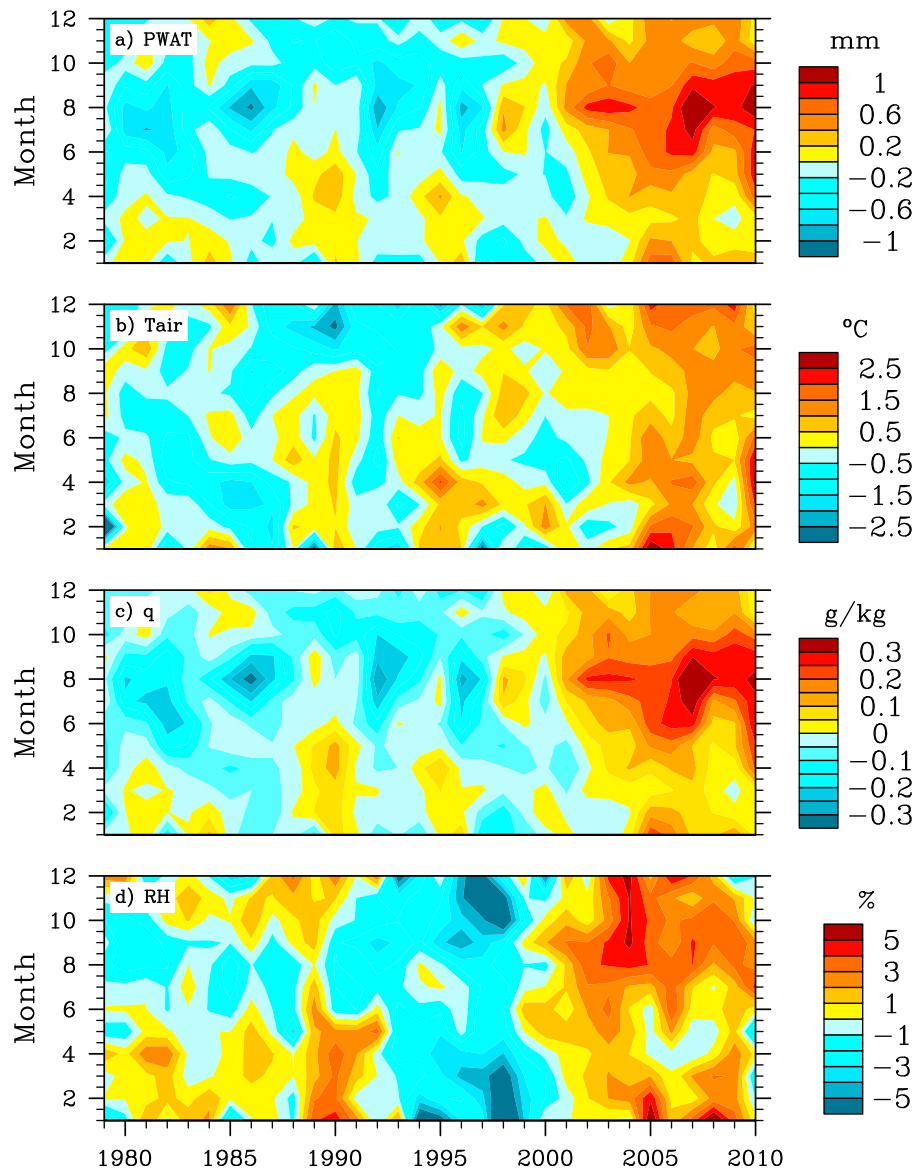


Figure 11. Anomalies by month and year for the region north of 70°N from MERRA data of (a) 1000 to 500 hPa precipitable water, (b) 850 hPa temperature, (c) 850 hPa specific humidity, and (d) 850 hPa relative humidity.

for the region north of 70°N of surface to 500 hPa precipitable water, 850 hPa air temperature, 850 hPa specific humidity and 850 hPa relative humidity. Anomalies are with respect to the full period of record, 1979–2010. The MERRA data depict generally negative anomalies in precipitable water from 1979 to 2000, but with considerable

variability over this period (note especially the positive anomalies in the late 1980s and early 1990s for spring), contrasting with mostly positive anomalies over the past decade. The strongest recent anomalies are found in summer and early autumn. Anomaly patterns for 850 hPa air temperature and 850 hPa specific humidity are similar.

Figure 10. Cross sections based on ERA-I data by height (vertical axis, up to 300 hPa) and latitude (horizontal axis) of (left column) anomalies in specific humidity for the decade 2001–2010 relative to 1979–2010 means (middle column), anomalies in specific humidity for 2001–2010 expressed as a percent change relative to 1979–2010 means, and (right column) anomalies in air temperature. The cross sections are for a transect extending from 60°N along the date line northward to 90°N and then along the prime meridian southward to 60°N. Anomalies in specific humidity exceeding 0.1 g kg⁻¹ (absolute values) are shown in color, as are anomalies larger than $\pm 5\%$. For temperature, anomalies that exceed 0.5°C in absolute magnitude are shown in color. The cross sections are provided for alternate months (January, March, May, July, September, and November).

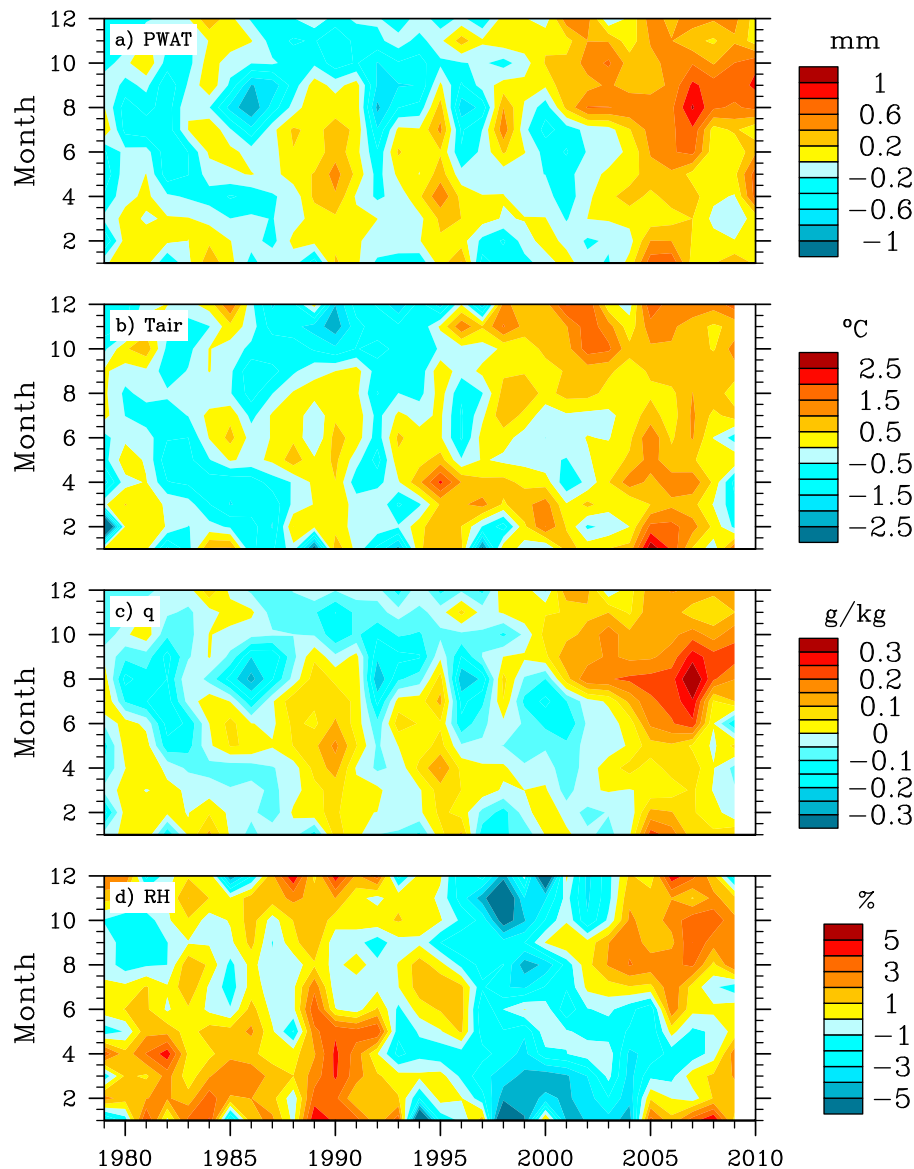


Figure 12. Anomalies by month and year for the region north of 70°N from CFSR data of (a) 1000 to 500 hPa precipitable water, (b) 850 hPa temperature, (c) 850 hPa specific humidity, and (d) 850 hPa relative humidity.

According to MERRA, relative humidity at the 850 hPa level has varied by about $\pm 5\%$ over the period of record, with a mix of positive and negative anomalies from 1979 through the early 1990s, negative anomalies in all months from the early 1990s through about of the century, and generally positive anomalies thereafter.

[38] We have no clear explanation for this decadal-scale shift from negative to positive relative humidity anomalies. Differences in atmospheric circulation were modest. While the decade 1991–2000 was characterized by slightly below average sea level pressure over the Arctic Ocean in the annual mean, contrasting with a mix of negative and positive anomalies for the decade 2001–2010, none of the Arctic anomalies exceed 1 hPa. Changes in data streams likely plays a role; as mentioned earlier, *Cullather and*

Bosilovich [2011] find that the MERRA moisture budget components are sensitive to introduction of AMSU data in November 1998. Another significant change was introduction of the AIRS instrument in 2002. With respect to data streams, the MERRA relative humidity plot also shows a clearly unphysical feature – a narrow band of positive anomalies (exceeding 5%) spanning September 2004 through February 2005.

[39] The temporal evolution for the polar cap in precipitable water, 850 hPa air temperature, specific humidity and relative humidity based on the CFSR records (Figure 12) is similar to that shown in MERRA, but there are also some notable differences. Peak positive anomalies on CFSR are smaller than in MERRA. The CFSR record does not have

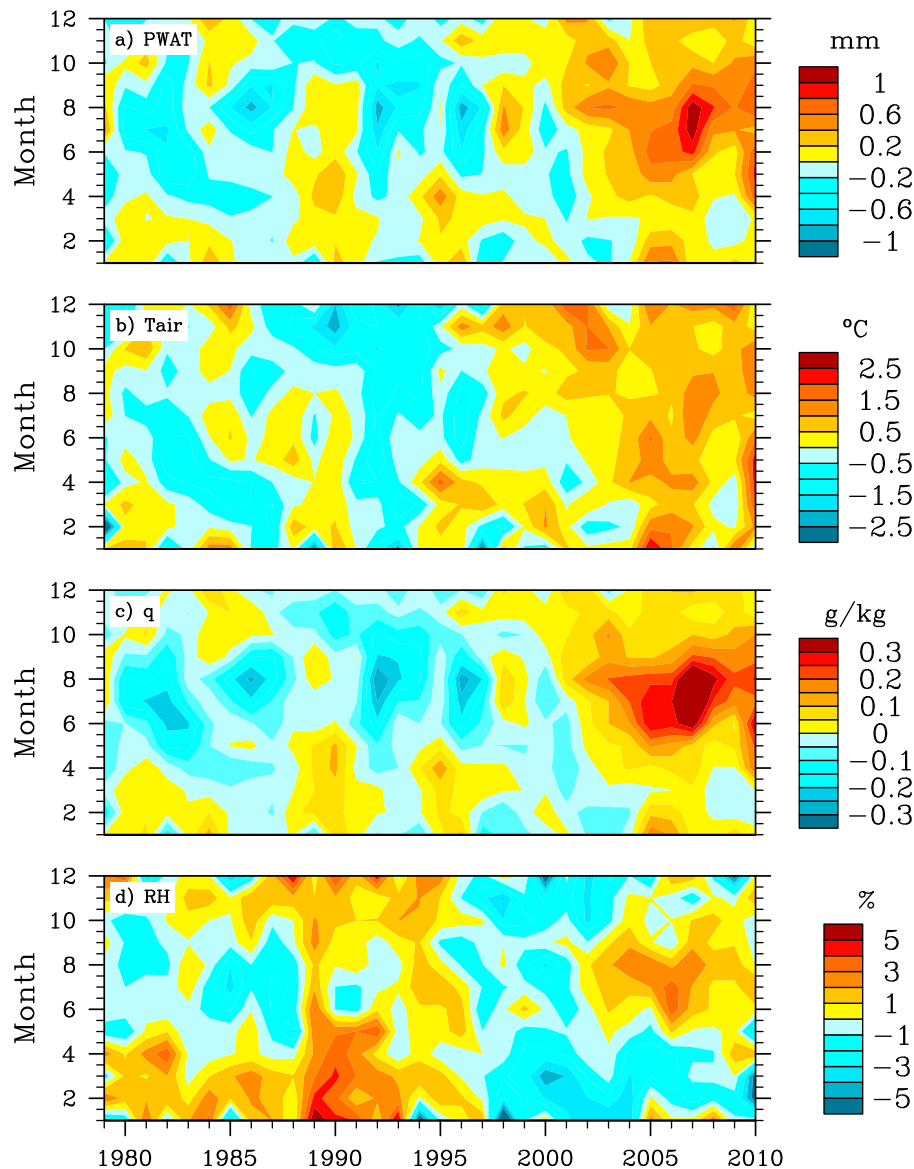


Figure 13. Anomalies by month and year for the region north of 70°N from ERA-I data of (a) 1000 to 500 hPa precipitable water, (b) 850 hPa temperature, (c) 850 hPa specific humidity, and (d) 850 hPa relative humidity.

the unphysical relative humidity feature seen in MERRA, nor does the ERA-I record (Figure 13).

5. Summary and Conclusions

[40] On the basis of radiosonde profiles and output from the three latest generation atmospheric reanalyses (MERRA, CFSR and ERA-I), statistically significant trends in precipitable water over the Arctic as assessed over the period 1979–2010 are mostly positive. Trends from the three reanalyses are variously larger or smaller than radiosonde-based estimates. Trends are highly heterogeneous in space and time. The most consistent pattern between months and between the reanalyses is increasing precipitable water over the open waters of the northern North Atlantic, consistent with observed increases in sea surface temperature. Increases

are also prominent over the Canadian Arctic Archipelago, especially in the summer months; the strong summer trends in this region are also seen in the radiosonde data. A feature common to all of the reanalyses is a region of positive trends in precipitable water centered over the Beaufort and Chuckchi seas in August and September, corresponding to where negative trends in end-of-summer summer sea ice extent have been most pronounced. These trend patterns mask considerable variability from year to year and from decade to decade.

[41] The results presented here must be viewed with the caveat of uncertainties in both the radiosonde and the reanalysis data. Obtaining accurate humidity data in polar regions from radiosondes has and will remain to be a daunting problem. Pointing to challenges of data assimilation in high latitudes, we have also shown that the reanalyses

have moist and warm biases at and near the surface from autumn through spring, with smaller biases in summer. None of the reanalyses correctly capture the cold season humidity and temperature inversions seen in the radiosonde data. There are some substantial differences between MERRA, CFSR and ERA-I with respect to the vertical structure of recent (2001–2010 decade) anomalies in specific humidity and air temperature. We see evidence of unphysical features in the MERRA record, and numerous past studies have identified a slate of potential inconsistencies related to changes in data streams.

[42] Our results are nevertheless consistent with a changing Arctic environment with a warmer atmosphere that can carry more water vapor, higher north Atlantic sea surface temperatures and reduced sea ice extent. Obvious next steps are to assess the contribution of increased water vapor to observed increases in Arctic surface air temperature via radiative transfer modeling and to examine whether changes in the availability of water vapor contribute to changes in high latitude precipitation.

[43] **Acknowledgments.** This study was supported by NSF grants ARC 0901962 and ARC 0805821, and by NASA grant NNX08AQ70G. M. Ishii provided JRA-25 reanalysis. A. Dai (NCAR) provided homogenized radiosonde data for Arctic sites.

References

- Andersson, E., et al. (2005), Assimilation and modeling of the atmospheric hydrologic cycle in the ECMWF forecasting system, *Bull. Am. Meteorol. Soc.*, *86*, 387–402, doi:10.1175/BAMS-86-3-387.
- Bromwich, D. H., R. L. Fogt, K. I. Hodges, and J. E. Walsh (2007), A tropospheric assessment of the ERA-40, NCEP, and JRA-25 global reanalyses in the polar regions, *J. Geophys. Res.*, *112*, D10111, doi:10.1029/2006JD007859.
- Cullather, R. L., and M. G. Bosilovich (2011), The moisture budget of the polar atmosphere in MERRA, *J. Clim.*, *24*, 2861–2879, doi:10.1175/2010JCLI4090.1.
- Dai, A. (2006), Recent climatology, variability, and trends in global surface humidity, *J. Clim.*, *19*, 3589–3606, doi:10.1175/JCLI3816.1.
- Dai, A., J. W. Wang, P. W. Thorne, D. E. Parker, L. Haimberger, and X. L. Wang (2011), A new approach to homogenize daily radiosonde humidity data, *J. Clim.*, *24*, 965–991, doi:10.1175/2010JCLI3816.1.
- Dee, D. P., et al. (2011), The ERA-Interim reanalysis: Configuration and performance of the data assimilation system, *Q. J. R. Meteorol. Soc.*, *137*, 553–597, doi:10.1002/qj.828.
- Devasthale, A., J. Sedlar, and M. Tjernström (2011), Characteristics of water-vapour inversions observed over the Arctic by Atmospheric Infrared Sounder (AIRS) and radiosondes, *Atmos. Chem. Phys.*, *11*, 9813–9823, doi:10.5194/acp-11-9813-2011.
- Durre, I., R. S. Vose, and D. B. Wuetz (2006), Overview of the integrated global radiosonde archive, *J. Clim.*, *19*, 53–68, doi:10.1175/JCLI3594.1.
- Elliott, W. P., and D. J. Gaffen (1991), On the utility of radiosonde humidity archived for climate studies, *Bull. Am. Meteorol. Soc.*, *72*, 1507–1520, doi:10.1175/1520-0477(1991)072<1507:OTUORH>2.0.CO;2.
- Francis, J. A., and A. Hunter (2007), Changes in the fabric of the Arctic's greenhouse blanket, *Environ. Res. Lett.*, *2*, 045011, doi:10.1088/1748-9326/2/4/045011.
- Garand, L. C., C. Grassotti, J. Halle, and G. Klein (1992), On differences in radiosonde humidity reporting practices and their implications for numerical weather prediction and remote sensing, *Bull. Am. Meteorol. Soc.*, *73*, 1417–1423, doi:10.1175/1520-0477(1992)073<1417:ODIRHR>2.0.CO;2.
- Holland, M. M., and C. M. Bitz (2003), Polar amplification of climate change in coupled models, *Clim. Dyn.*, *21*, 221–232, doi:10.1007/s00382-003-0332-6.
- Kalnay, E., et al. (1996), The NCEP/NCAR 40-year reanalysis project, *Bull. Am. Meteorol. Soc.*, *77*, 437–471, doi:10.1175/1520-0477(1996)077<0437:TNYRP>2.0.CO;2.
- Manabe, S., and R. J. Stouffer (1980), Sensitivity of a global climate model to an increase of CO₂ in the atmosphere, *J. Geophys. Res.*, *85*(C10), 5529–5554, doi:10.1029/JC085iC10p05529.
- Maslanik, J. A., C. Fowler, J. Stroeve, S. Drobot, H. J. Zwally, D. Yi, and W. J. Emery (2007), A younger, thinner ice cover: Increased potential for rapid, extensive ice loss, *Geophys. Res. Lett.*, *34*, L24501, doi:10.1029/2007GL032043.
- McCarthy, M. P., P. W. Thorne, and H. A. Tichner (2009), An analysis of tropospheric humidity trends from radiosondes, *J. Clim.*, *22*, 5820–5838, doi:10.1175/2009JCLI2879.1.
- Nghiem, S. V., Y. Chao, G. Neumann, P. Li, D. K. Perovich, T. Street, and P. Clemente-Colon (2006), Depletion of perennial sea ice in the east Arctic Ocean, *Geophys. Res. Lett.*, *33*, L17501, doi:10.1029/2006GL027198.
- Onogi, K., et al. (2007), The JRA-25 reanalysis, *J. Meteorol. Soc. Jpn.*, *85*, 369–432, doi:10.2151/jmsj.85.369.
- Overland, J. E., and M. Wang (2010), Large-scale atmospheric circulation changes are associated with the recent loss of Arctic sea ice, *Tellus, Ser. A*, *62*, 1–9.
- Philippa, R., B. Dürr, A. Ohmura, and C. Ruckstuhl (2005), Anthropogenic greenhouse forcing and strong water vapor feedback increase temperature in Europe, *Geophys. Res. Lett.*, *32*, L19809, doi:10.1029/2005GL023624.
- Randel, D. L., T. H. Vonder Haar, M. A. Ringerud, G. L. Stephens, T. J. Greenwald, and C. L. Coombs (1996), A new global water vapor dataset, *Bull. Am. Meteorol. Soc.*, *77*, 1233–1246, doi:10.1175/1520-0477(1996)077<1233:ANGWVD>2.0.CO;2.
- Rawlins, M. A., et al. (2010), Analysis of the Arctic system for freshwater cycle intensification: Observations and expectations, *J. Clim.*, *23*, 5715–5737, doi:10.1175/2010JCLI3421.1.
- Rienecker, M. M., et al. (2011), MERRA—NASA's Modern-Era Retrospective Analysis for Research and Applications, *J. Clim.*, *24*, 3624–3648, doi:10.1175/JCLI-D-11-00015.1.
- Rinke, A., C. Melsheimer, K. Dethloff, and G. Heygster (2009), Arctic total water vapor: Comparison of regional climate simulations with observations, and simulated decadal trends, *J. Hydrometeorol.*, *10*, 113–129, doi:10.1175/2008JHM970.1.
- Ross, R. J., and W. P. Elliott (2001), Radiosonde-based northern hemisphere tropospheric water vapor trends, *J. Clim.*, *14*, 1602–1612, doi:10.1175/1520-0442(2001)014<1602:RBNHTW>2.0.CO;2.
- Saha, S., et al. (2010), The NCEP Climate Forecast System Reanalysis, *Bull. Am. Meteorol. Soc.*, *91*, 1015–1057, doi:10.1175/2010BAMS3001.1.
- Screen, J. A., and I. Simmonds (2010a), The central role of diminishing sea ice in recent Arctic temperature amplification, *Nature*, *464*, 1334–1337, doi:10.1038/nature09051.
- Screen, J. A., and I. Simmonds (2010b), Increasing fall winter energy loss from the Arctic Ocean and its role in Arctic amplification, *Geophys. Res. Lett.*, *37*, L16707, doi:10.1029/2010GL044136.
- Serreze, M. C., R. G. Barry, and J. E. Walsh (1995), Atmospheric water vapor characteristics at 70°N, *J. Clim.*, *8*, 719–731, doi:10.1175/1520-0442(1995)008<0719:AWVCA>2.0.CO;2.
- Serreze, M. C., A. P. Barrett, D. N. Kindig, and M. M. Holland (2009), The emergence of surface-based Arctic amplification, *Cryosphere*, *3*, 11–19, doi:10.5194/tc-3-11-2009.
- Serreze, M. C., A. P. Barrett, and J. J. Cassano (2011), Circulation and surface controls on the lower tropospheric air temperature field of the Arctic, *J. Geophys. Res.*, *116*, D07104, doi:10.1029/2010JD015127.
- Simpson, J. J., J. S. Berg, C. J. Kobinski, G. L. Hufford, and B. Beckley (2001), The NVAP global water vapor dataset: Independent cross comparison and multi-year variability, *Remote Sens. Environ.*, *76*, 112–129, doi:10.1016/S0034-4257(00)00199-1.
- Soden, B. J., R. T. Wetherald, G. L. Stenchikov, and A. Robock (2002), Global cooling after the eruption of Mount Pinatubo: A test of climate feedback by water vapor, *Science*, *296*, 727–730, doi:10.1126/science.296.5568.727.
- Soden, B. J., D. N. Jackson, V. Ramaswamy, M. D. Schwarzkopf, and X. Huang (2005), The radiative signature of upper tropospheric moistening, *Science*, *310*, 841–844, doi:10.1126/science.1115602.
- Solomon, S., K. H. Rosenlof, R. W. Portmann, J. S. Daniel, S. M. Davis, T. J. Sanford, and G.-K. Plattner (2010), Contributions of stratospheric water vapor to decadal changes in the rate of global warming, *Science*, *327*, 1219–1223, doi:10.1126/science.1182488.
- Stroeve, J., M. Serreze, S. Drobot, S. Gearheard, M. Holland, J. Maslanik, W. Meier, and T. Scambos (2008), Arctic sea ice extent plummets in 2007, *Eos Trans. AGU*, *89*, 13–14, doi:10.1029/2008E002001.
- Stroeve, J. C., M. C. Serreze, A. P. Barrett, and D. N. Kindig (2011), Attribution of recent changes in autumn cyclone associated precipitation in the Arctic, *Tellus, Ser. A*, *63*(4), 653–663, doi:10.1111/j.1600-0870.2011.00515.x.
- Trenberth, K. E., J. Fasullo, and L. Smith (2005), Trends and variability in column integrated atmospheric water vapor, *Clim. Dyn.*, *24*, 741–758, doi:10.1007/s00382-005-0017-4.
- Uppala, S., et al. (2005), The ERA-40 re-analysis, *Q. J. R. Meteorol. Soc.*, *131*, 2961–3012, doi:10.1256/qj.04.176.

- Walsh, J. E., X. Zhou, D. Portis, and M. C. Serreze (1995), Atmospheric contribution to hydrologic variations in the Arctic, *Atmos. Ocean*, *34*, 733–755.
- Wang, J., D. J. Carlson, D. B. Parsons, T. F. Hock, D. Lauritsen, H. L. Cole, K. Beierle, and E. Chamberlain (2003), Performance of operational radiosonde humidity sensors in direct comparison with a chilled mirror dew-point hydrometer and its climate implication, *Geophys. Res. Lett.*, *30*(16), 1860, doi:10.1029/2003GL016985.
- Wentz, F. J. (1997), A well-calibrated ocean algorithm for Special Sensor Microwave/Imager, *J. Geophys. Res.*, *102*(C4), 8703–8718, doi:10.1029/96JC01751.